Supplement of Atmos. Chem. Phys., 26, 11645–11666, 2026
https://doi.org/10.5194/acp-26-11645-2026-supplement

Atmospheric Chemistry and Physics
Open Access

Supplement of

Radar data shows graupel and increased turbulence near small-scale intermittent lightning discharges at the top of intense thunderstorms

Reinaart van Loon et al.

Correspondence to: Reinaart van Loon (reinaart.vanloon@wur.nl)

S1 Processing ψ_{dp} radar data

The cumulative differential phase ψ_{dp} is included in the Borkum radar dataset. We use the ωradlib Python package (Heistermann et al., 2013) for filtering and computing the differential phase shift ϕ_{dp} and the specific differential phase K_{dp} values. The result is highly depend on filtering and correction choices.

In general, ψ_{dp} is noisy. The approach that is used to retrieve meaningful ϕ_{dp}-values and to compute K_{dp}, follows the method as described by Vulpiani et al. (2012b). The described method is an iterative process based upon four steps:

1. K_{dp} is calculated using a finite difference method on the ψ_{dp} signal: K'_{dp}
2. K_{dp} values are filtered for realistic values such that $\kappa_1 < K'_{dp} < \kappa_2$. When this condition is not met, K'_{dp} is replaced with a zero value. This method attempts to remove noise and backscatter phase δ_{hv}. Potential phase folding should be taken into account to prevent unnecessary data loss.
3. $\hat{\phi}_{dp}$ is reconstructed by integration of the filtered K'_{dp}.
4. K_{dp} is computed from $\hat{\phi}_{dp}$: $\hat{K}_{dp}$

It is important to realize that the computation of K_{dp} uses a smoothing window. This has a twofold purpose. Not only does it smooth the noisy ψ_{dp} signal, it also deals with values outside the $\kappa_1 - \kappa_2$ range. Once the $\kappa_1 < K'_{dp} < \kappa_2$ is not met, K'_{dp} values are replaced by zero's. These nonphysical zero values are compensated by smoothing of the neighbouring values. For this reason, Vulpiani et al. (2012b) suggests to iterate over steps 3 and 4.

Another important artifact to consider is that phase measurements are prone to phase folding. The phase measurements are limited to $180°$, such that when a phase shift is increased beyond $180°$, it jumps to $-180°$. The opposite holds for the phase decreasing from $-180°$, that results in a jump to $180°$. Phase jumps always lead to K'_{dp} values outside the $\kappa_1 - \kappa_2$ range and subsequently data loss. Therefore, it is useful to try to unfold the phase folds into a useful signal.

Although powerful because of the smoothing, and because of the independence of ψ_{dp} calibration offsets, the method by Vulpiani et al. (2012b) in the`wradlib.dp.phidp_kdp_vulpiani` function has a major shortcoming during phase unfolding. The unfolding is based on K'_{dp} computed with a central finite difference method. This method duplicates unwanted artifacts around the artifact itself. This may lead to unforeseen phase unfolding. Moreover, the suggested unfolding algorithm only permits for a single, $180°$ addition, to correct for phase folding. Therefore, it cannot cope with multiple folds or a fold in the decreasing $-180°$ direction. In such cases, data is lost because of the $\kappa_1 < K'_{dp} < \kappa_2$ restriction on K_{dp} in step 2. Finally, the Vulpiani et al. (2012b) method does not include possibilities for noise masks. The iteration of smoothed k_{dp} does compensate somewhat for random noise. However, the correction for the phase fold takes place before the smoothing.

To increase the performance on phase folds, we applied the following algorithm for ψ_{dp} processing:

1. Changes in ψ_{dp} are neglected for low reflectivity values. E.g. where $Z_h < z'$ or $Z_v < z'$.
2. Phase unfolding by a modified `wradlib.dp._unfold_phidp_naive` Python function based on Wang and Chandrasekar (2009). This algorithm differentiates between noise and actual phase folds, by comparing ρ_{hv} and the preceding

standard deviation. We modified the algorithm in order to tune the thresholds on the realistic propagation specific phase κ_1 and κ_2, the threshold for fold recognition K_{fold}, and the threshold for the maximum standard deviation σ_w.

3. K_{dp} values are filtered for realistic values such that $\kappa_1 < K'_{dp} < \kappa_2$. When this condition is not met, K'_{dp} is replaced with a zero value.
4. $\hat{\phi}_{dp}$ is reconstructed by integration of the filtered K'_{dp}.
5. K_{dp} is computed from $\hat{\phi}_{dp}$: $\hat{K}_{dp}$

For this study, the values for the filtering parameters in the above method are: $\kappa_1 = -5°$, $\kappa_2 = 20°$, $z' = 0$ dB, $\sigma_w = 0.8$. The size of the rolling window, for computation along the radar beam is 11 bins.

S2 Sensitivity tests

Figures S2.1–S2.4 show sensitivity tests of the data. Comparing respectively: the data in different altitude layers; the sensitivity to changing the radius to collect radar data near VHF sources; the clustering parameters for finding large lightning structures; and the clustering parameters for finding sparkle clusters.

S3 LOFAR images

Figures S3.1–S3.3 show LOFAR images with sparkle classification, zoomed-in on particular convective systems. They illustrate the nature of sparkles, as clouds of intermittent small-scale lightning discharges at high altitudes, and the performance of the sparkle classification algorithm. This is only a subset of all the LOFAR data used in this study.

S4 Radar images

Figures S4.1 and S4.2 show radar images of different radar variables of convective cell A and B, for times corresponding to LOFAR images.

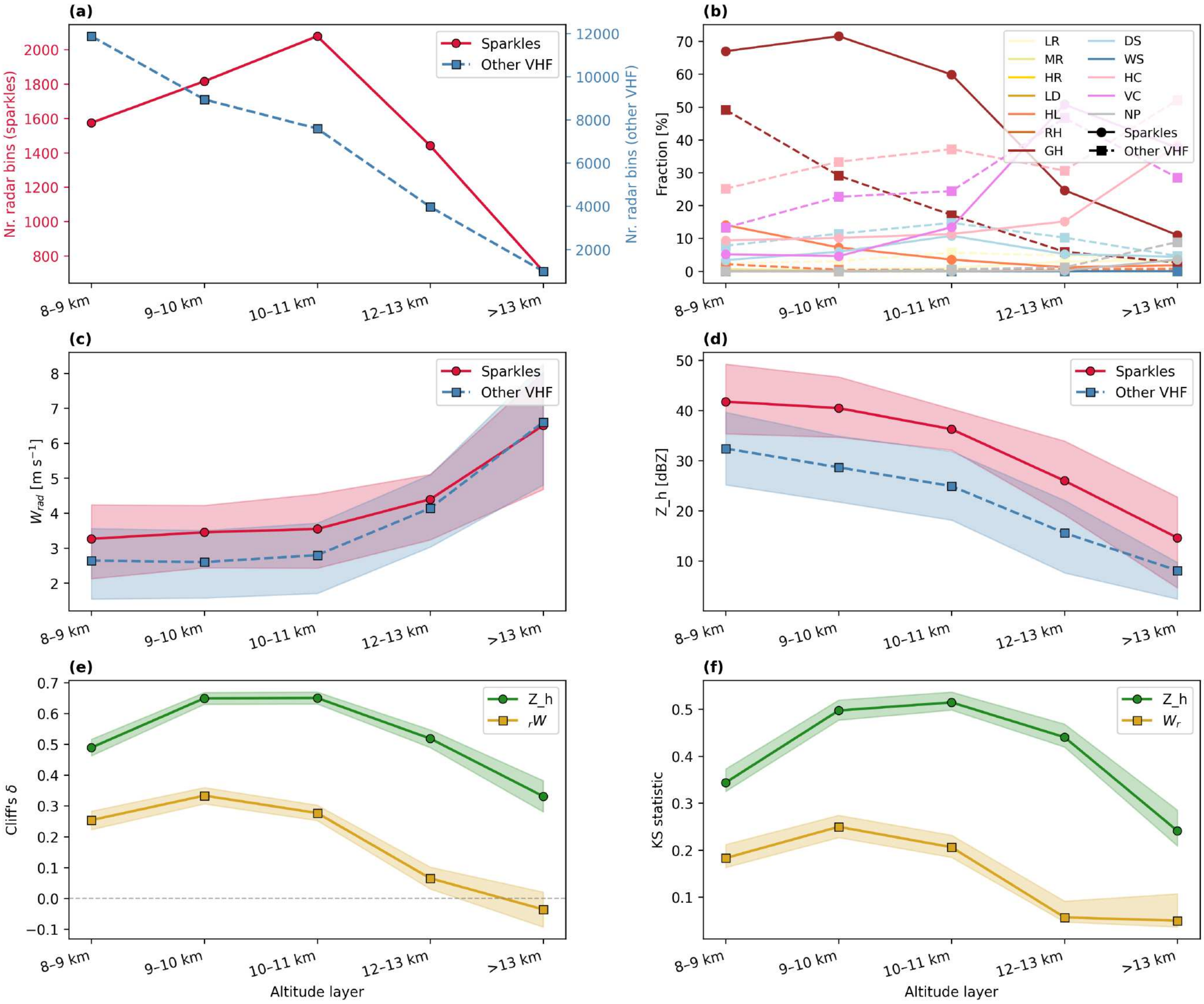

Figure S2.1. Comparing sparkles data to data near other VHF sources, in different altitude layers. (a) Number of radar points near sparkles (red circles, solid line) and near other VHF sources (blue squares, dashed line). (b) Fraction of the data in different HMC (hydrometeor classification) categories. (c) Mean W_{rad} values and with shading indicating the interquartile range. (d) Mean Z_h values and interquartile ranges. (e) Cliff's δ between the distribution of sparkles versus the distribution of other VHF sources. Green for Z_h distributions, and yellow for W_{rad} distributions. Shading shows the 95% confidence intervals of Cliff's δ based on a bootstrapping method.

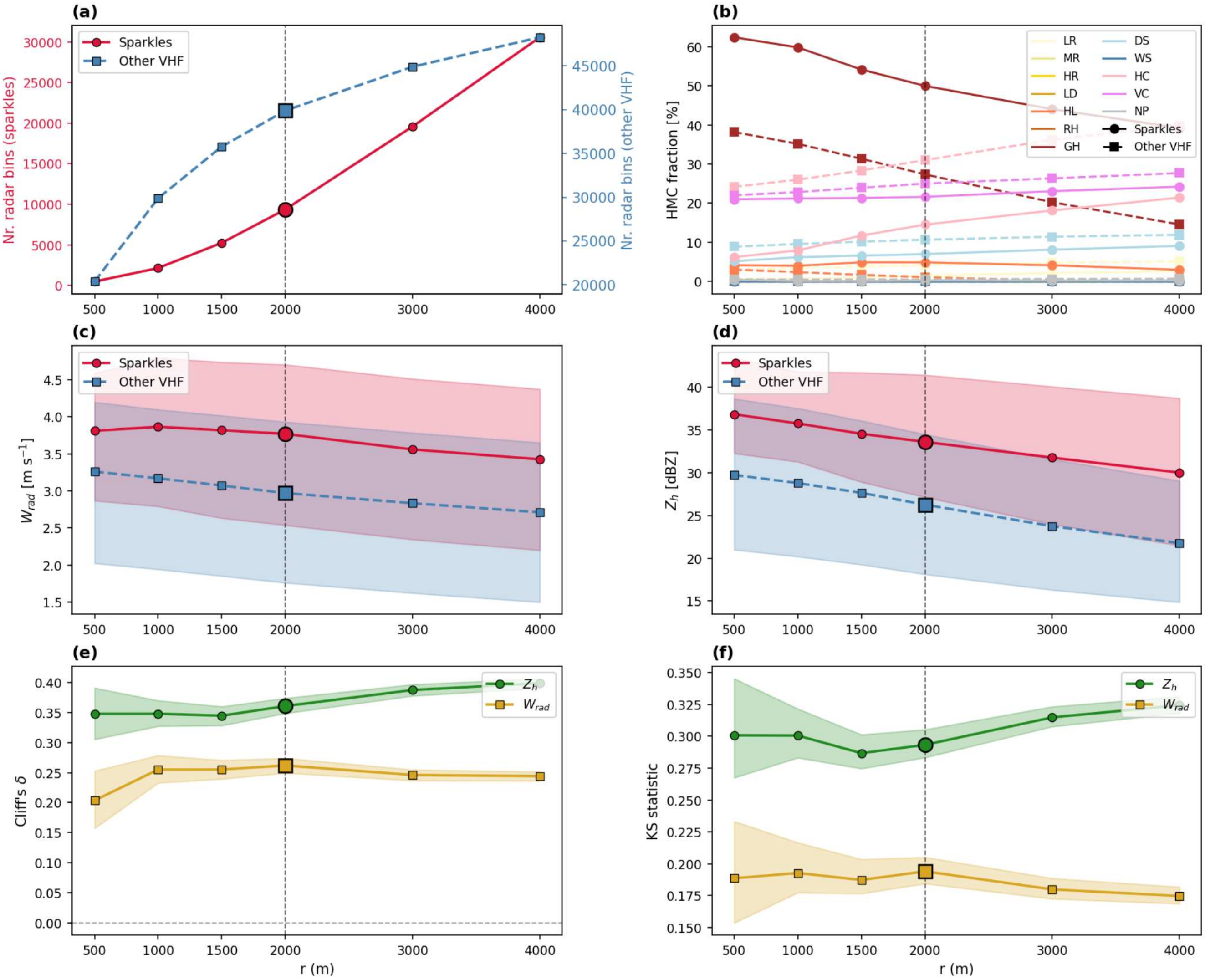

Figure S2.2. Sensitivity test of the radius r to collect radar data near VHF sources. (a) Number of radar points near sparkles (red circles, solid line) and near other VHF sources (blue squares, dashed line). (b) Fraction of the data in different HMC (hydrometeor classification) categories. (c) Mean W_{rad} values and with shading indicating the interquartile range. (d) Mean Z_h values and interquartile ranges. (e) Cliff's Delta between the distribution of sparkles versus the distribution of other VHF sources. Green for Z_h distributions, and yellow for W_{rad} distributions. Shading shows the 95% confidence intervals of Cliff's δ based on a bootstrapping method. (f) Kolmogorov-Smirnov (KS) test statistic between sparkles and other VHF distributions. Shading indicates the 95% confidence interval from a bootstrapping method.

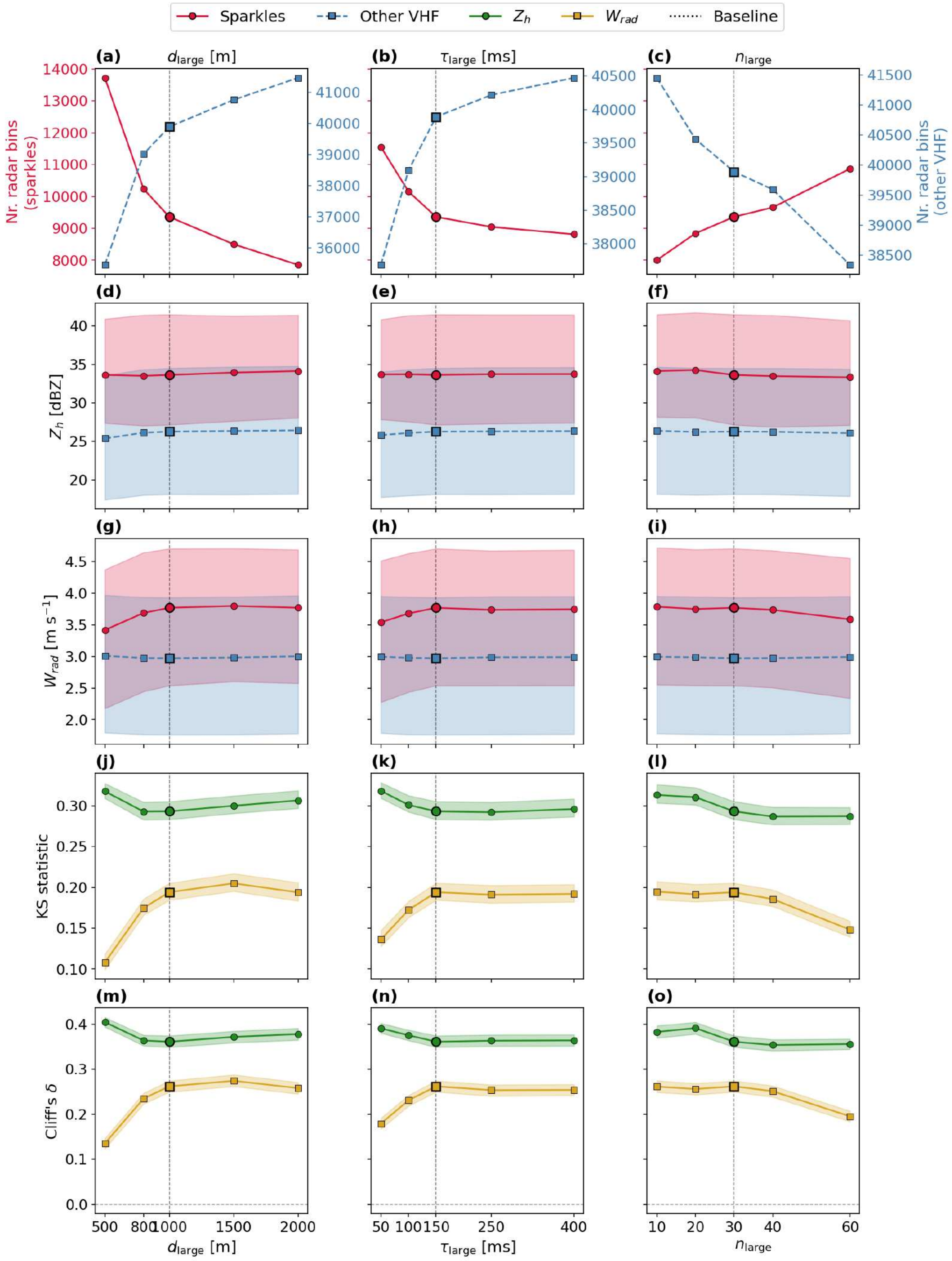

Figure S2.3. Sensitivity of the radar data, comparing sparkles to other VHF sources, to the parameters of the large-scale clustering of the sparkle classification algorithm. a-c) Number of radar data point near sparkles and other VHF sources (on different vertical scales. d-f) Mean Z_h values and interquartile range (shading). g-i) Mean W_{rad} values and interquartile range (shading). j-l) KS-statistic and 95% confidence interval (shading) from a bootstrap method. m-o) Cliff's δ and 95% confidence interval (shading). The spatial normalization factor, temporal normalization factor and the minimum number of sources, for the clustering of large lighting structures (d_{large}, τ_{large}, and n_{large} respectively), are varied from the baseline (values in Table 1 of revised manuscript) in each of the columns.

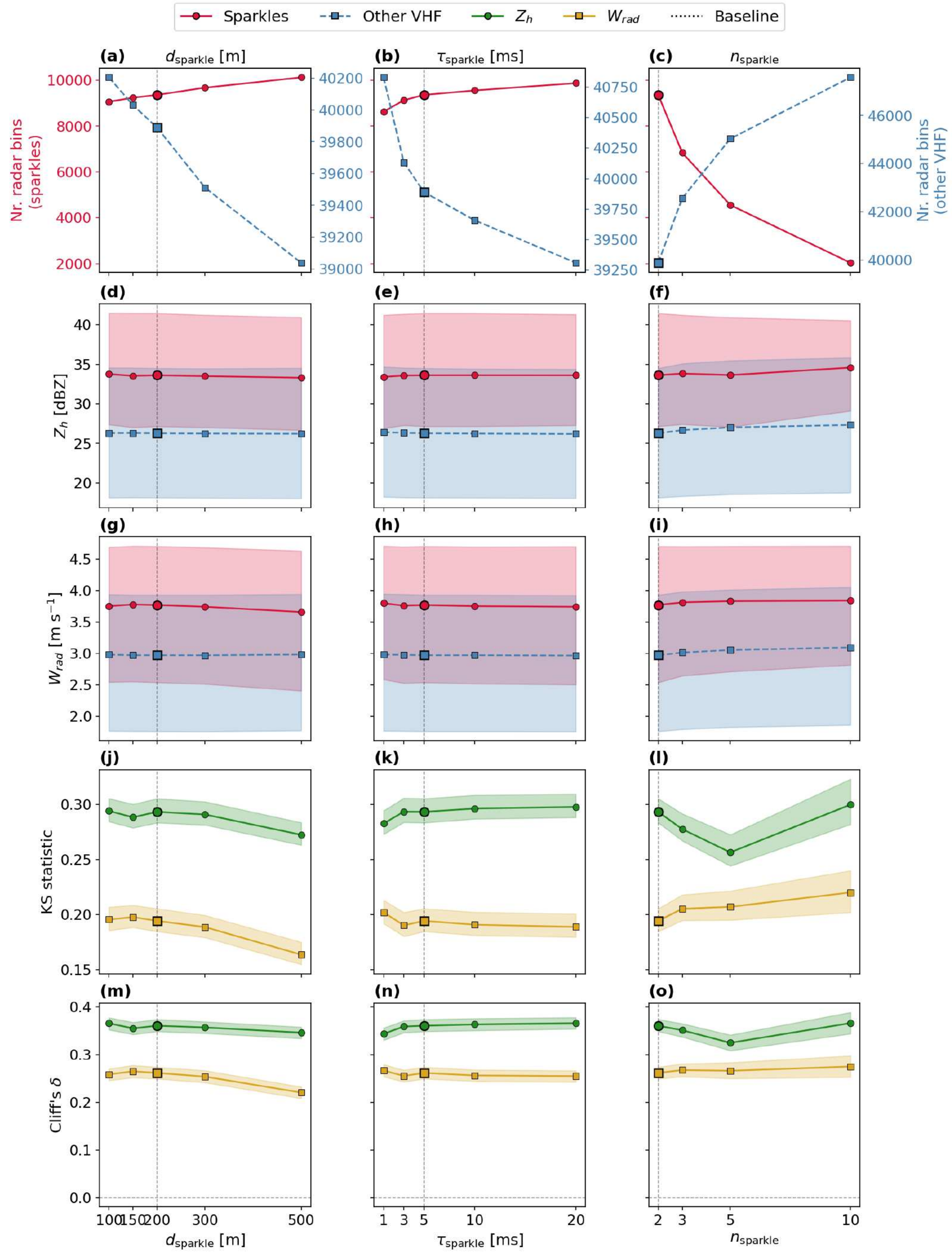

Figure S2.4. Similar to Fig. S2.3, but varying the spatial normalization factor, temporal normalization factor and the minimum number of sources, for the clustering of sparkles ($d_{sparkle}$, $\tau_{sparkle}$, and $n_{sparkle}$ respectively).

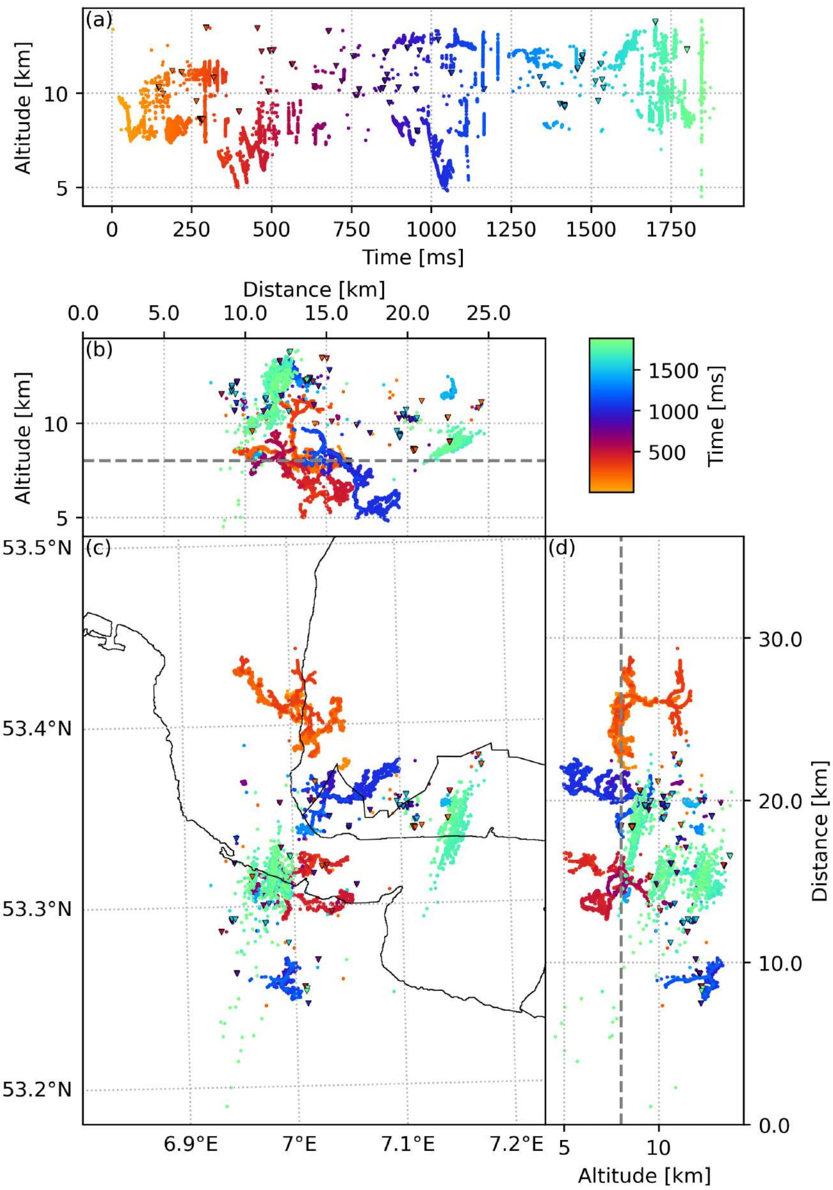

Figure S3.1. Similar to Fig. 2, but part of the LOFAR image at 19:17:36. The horizontal extent of panel (c) matches with Fig. 10. The gray dashed lines in panel (b) and (c) indicate the 8 km altitude threshold for sparkle selection.

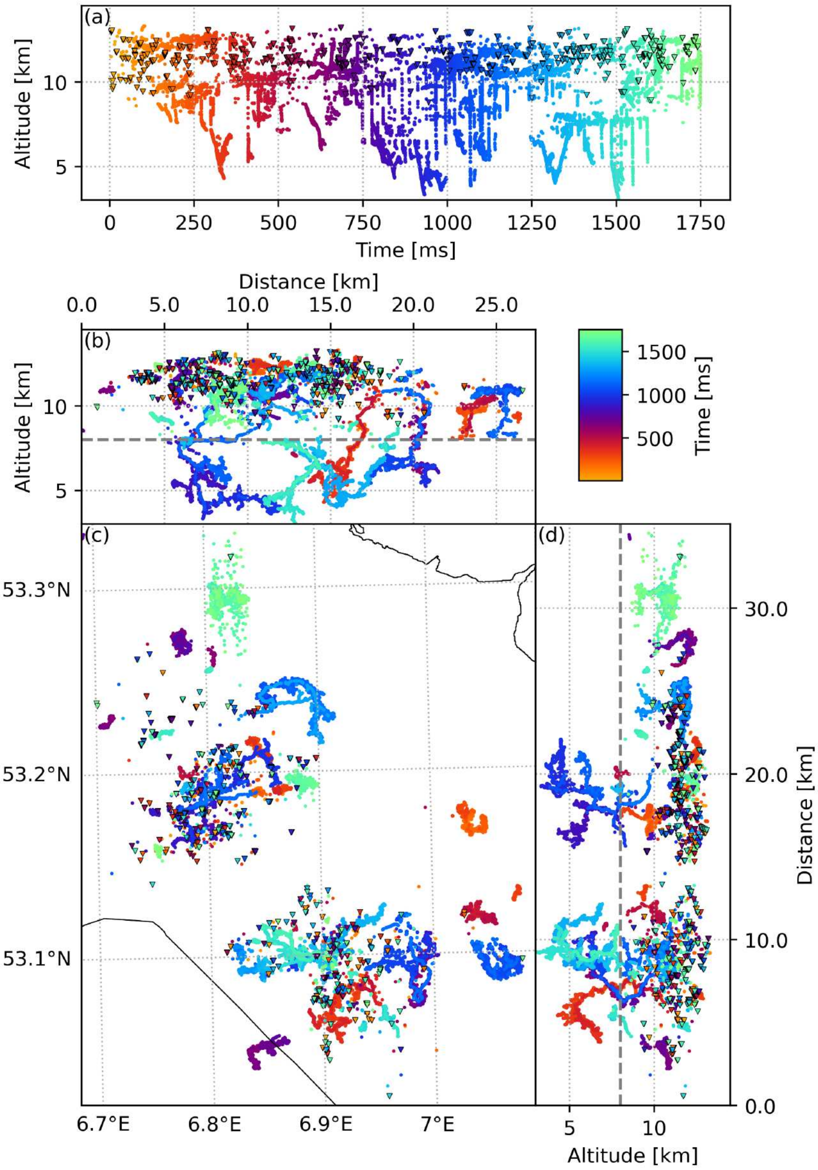

Figure S3.2. Similar to Fig. S3.1, but part of the LOFAR image at 19:37:29, and focusing of convective system B.

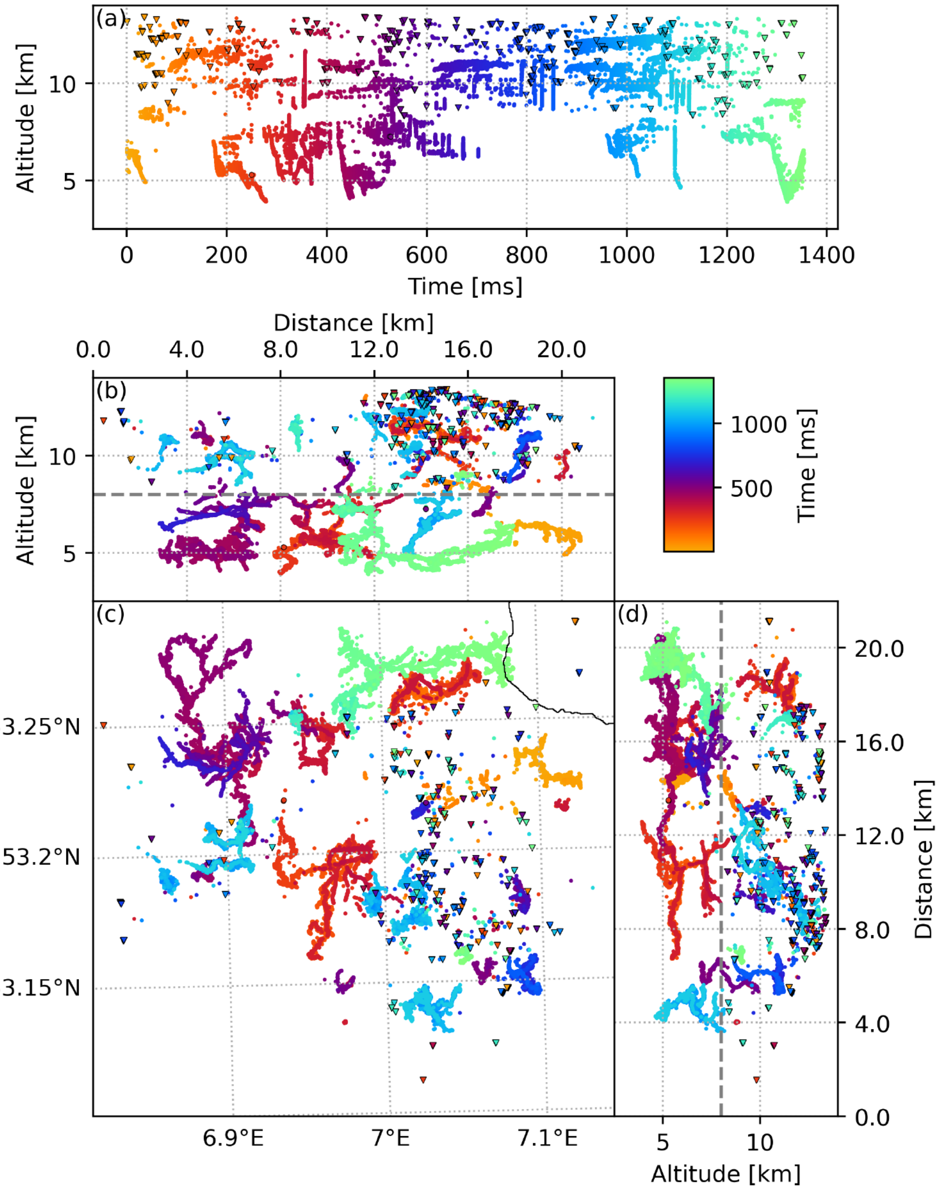

Figure S3.3. Similar to Fig. S3.1, but part of the LOFAR image at 19:54:24, and focusing on convective system B. The horizontal extent of panel (c) matches with Fig. 1. The VHF sources with a point shape and black contour are marked as sparkles by the two-stage clustering process, but fall below the 8 km altitude threshold.

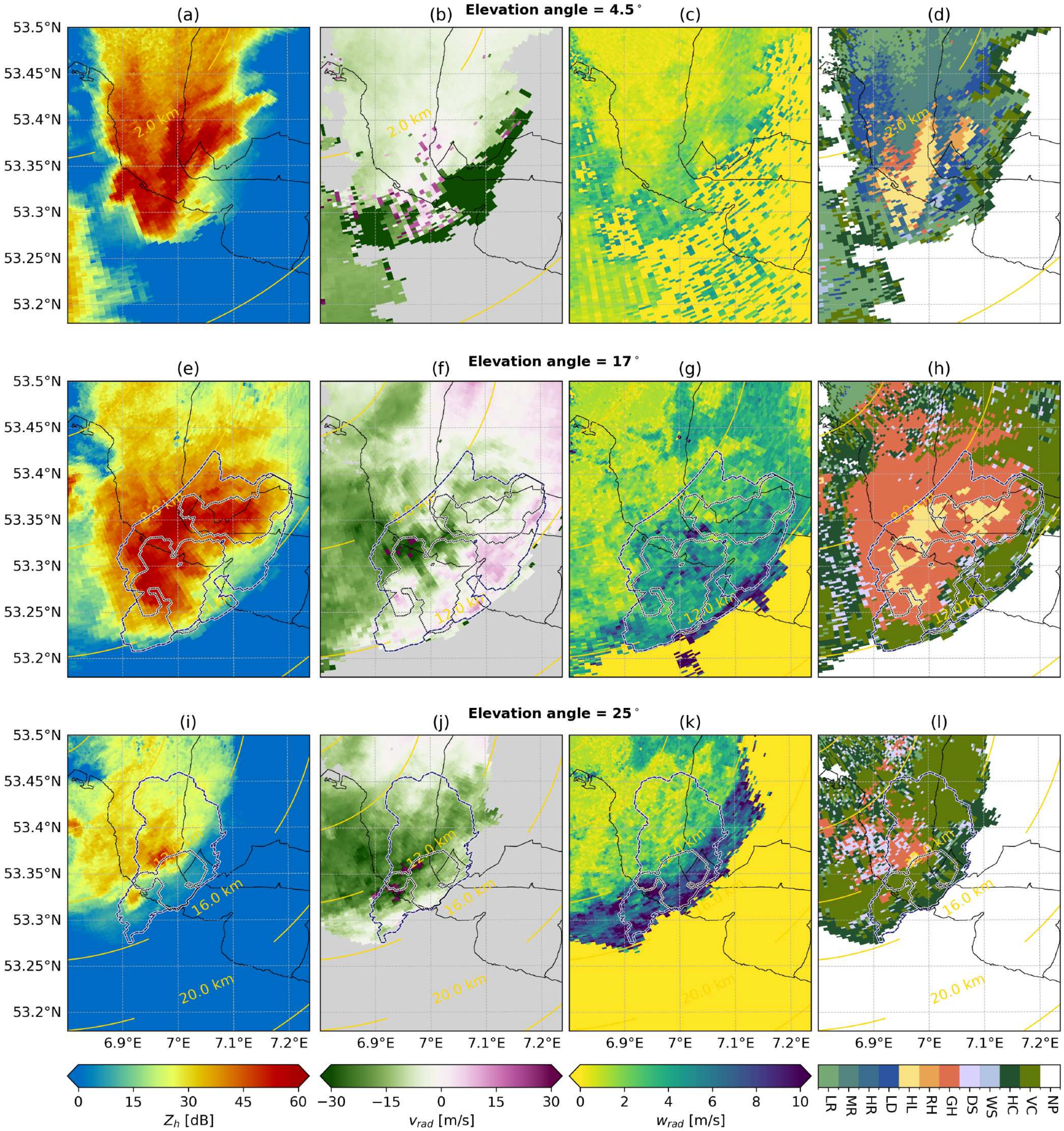

Figure S4.1. Similar to Fig. 10, but comparing different radar elevation angles (4.5°, 17°, and 25° in rows 1–3 respectively). Panels in the same column share the same variable (Z_h, V_{rad}, W_{rad}, and HMC) and color bar at the bottom.

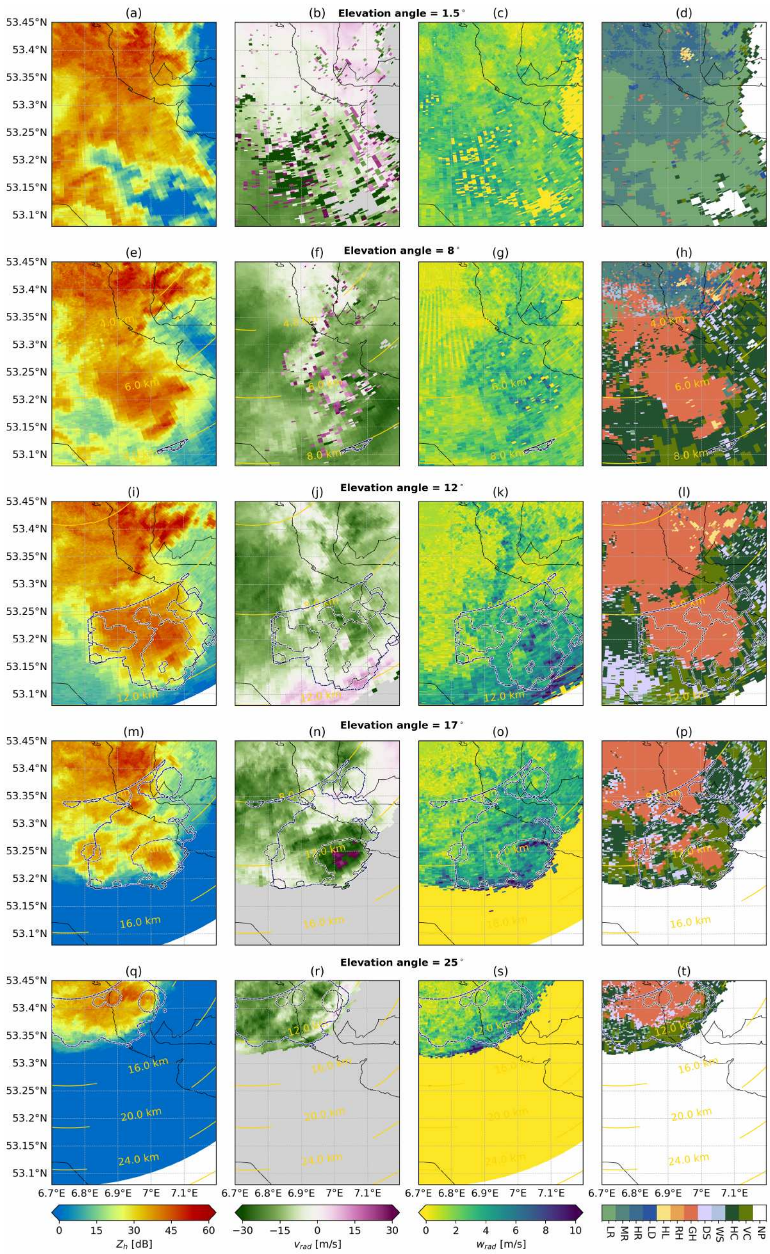

Figure S4.2. Similar to Fig. 11 and Fig. 11, but comparing different radar elevation angles (1.5°, 8°, 12°, 17°, and 25° in rows 1–5 respectively). Panels in the same column share the same variable (Z_h, V_{rad}, W_{rad}, and HMC) and color bar at the bottom.